RSC Advances

ROYAL SOCIETY
OF CHEMISTRY

PAPER

View Article Online
View Journal | View Issue

Cite this: *RSC Adv.*, 2026, **16**, 9246

A new multifunctional one-dimensional bromo-bismuthate(III): synthesis, structural features, characterization, and optical properties of $(C_{10}H_{13}N_4)[BiBr_4]\cdot 2H_2O$

Amin Alibi,[a] Sameh Sellami,[b] Nour Elleuch,[a] Sergiu Shova,[d] Fakher Chabchoub[c] and Mohamed Boujelbene *[a]

A new one-dimensional bromobismuthate(III) organic–inorganic hybrid $(C_{10}H_{13}N_4)[BiBr_4]\cdot 2H_2O$, was successfully synthesized and comprehensively investigated to elucidate its structural, thermal, and optoelectronic characteristics. Single-crystal X-ray diffraction established a monoclinic system ($P2_1/n$) with one-dimensional $[BiBr_4]_n^{n-}$ chains composed of edge-sharing $BiBr_6$ octahedra, stabilized through an extended network of hydrogen bonding and π–π stacking interactions. Vibrational spectroscopy (FTIR and Raman) confirmed the coexistence and coupling of organic–inorganic subunits, while thermogravimetric analysis demonstrated excellent stability up to 275 °C, underscoring its robustness for high-temperature applications. Optical studies combining UV-vis, diffuse reflectance spectroscopy (DRS), and steady-state photoluminescence (PL) revealed a broad emission centered near 400 nm and an indirect band gap (E_g = 2.57 eV), as supported by TD-DFT calculations. These results confirm the compound's semiconducting behavior governed by the strong spin–orbit coupling of Bi(III), which induces band splitting and phonon-assisted transitions. The CIE 1976 chromaticity analysis located the emission within the blue–violet region ($u' = 0.1725$, $v' = 0.2513$), indicating high color purity and strong luminescence. This integrated experimental–theoretical approach demonstrates that $(C_{10}H_{13}N_4)[BiBr_4]\cdot 2H_2O$ is a stable, wide-band-gap, indirect semiconductor with promising potential for blue-emitting optoelectronic, photonic, and photovoltaic applications.

Received 6th December 2025
Accepted 3rd February 2026

DOI: 10.1039/d5ra09435f

rsc.li/rsc-advances

1. Introduction

Bismuth-based organic–inorganic hybrid materials have attracted significant research interest in recent years,[1] driving advancements in solar energy utilization,[2–5] nonlinear optical devices,[6,7] LEDs,[8,9] photoconductors,[10] optical microcavities,[11] and thin-film field-effect transistors.[12] These materials exhibit unique physical properties, making them promising alternatives to lead-based hybrid halometalates, which suffer from toxicity and instability. To address these limitations, researchers have explored the influence of different anionic configurations, including single or double chains,[13] zigzag chains,[14] ring-containing chains,[15] and spiral chains.[16,17] Among these, 1D halobismuthates ($ABiX_4$) have emerged as a promising class of materials.

Bismuth, like lead, possesses an outer $6s^2$ lone pair but is considerably less toxic due to the low solubility of its salts, preventing absorption. Additionally, its demulcent and protective properties further contribute to its biocompatibility. However, Bi-based materials suffer from low photoelectric efficiency, a key challenge that remains poorly understood.[18] Recent studies suggest that inducing internal chemical pressure *via* cation alloying and size mismatches could enhance performance.[19] Hybrid materials incorporating Bi^{3+} tend to form 1D or 2D structures,[20,21] and improving charge transfer within these materials has shown potential for enhancing their photoelectric properties. Various electron transport pathways, including X_2 molecules, X_2 ions, HX molecules, water molecules, and solvent interactions, have been explored to optimize performance.

Halobismuthates exhibit diverse structural configurations, including zero-dimensional (0D) clusters ($[BiCl_6]^{3-}$, $[Bi_2Br_9]^{3-}$ $[Bi_2Cl_{11}]^{5-}$, *etc.*), one-dimensional (1D) chains ($[BiI_4]^-$, $[BiI_5]^{2-}$ $[Bi_2I_7]^-$, *etc.*), and two-dimensional (2D) networks ($[Bi_2Br_9]^{3-}$ $[Bi_{2/3}I_4]^{2-}$).[14,22] The negative charge of halobismuthates is balanced by organic cations *via* electrostatic forces, hydrogen

---

[a] Laboratory of Physico-Chemistry of Solid State, LR11ES51, Sfax Faculty of Sciences, University of Sfax, Sfax 3000, Tunisia. E-mail: m_boujelbene2010@yahoo.fr

[b] Biopesticides Laboratory, Centre of Biotechnology of Sfax, Sfax University, P.O. Box '1177' 3018, Sfax, Tunisia

[c] Applied Chemistry Laboratory: Heterocycles, Fats and Polymers, Faculty of Sciences of Sfax, Sfax 3000, Tunisia

[d] "Petru Poni" Institute of Macromolecular Chemistry, Alea Grigore Ghica voda 41-A, 700487 Iasi, Romania

bonding, and van der Waals interactions, influencing the final material properties.[23] Despite extensive structural studies, research on their optoelectronic properties remains limited.[24] Some halobismuthates have demonstrated potential as active layers in photovoltaic devices[25,26] due to their inherent stability, though their efficiency remains low.[27] Additionally, specific Bi/halide ratios (*e.g.*, Bi_0X_9, BiX_5, Bi_2X_{11}) influence electrical and optical properties, with some compositions exhibiting ferroelectric behavior.[28,29] However, achieving precise control over the Bi/halide ratio remains challenging due to reaction conditions, stoichiometry, and the stabilizing role of organic cations.

Efforts to increase the dimensionality of bismuth-based hybrid materials have led to the formation of 1D bromobismuthate networks, including rare Bi/Br compositions such as $[BiBr_4]^-$ and $[BiBr_5]^{2-}$. In this study, we incorporated the 5-Amino-3-ethyl-1-phenyl-1*H*-1,2,4-triazole ($C_{10}H_{12}N_4$) organic molecule into a Bi-based hybrid framework to synthesize the photoactive bromobismuthate $(C_{10}H_{13}N_4)[BiBr_4]\cdot 2H_2O$. We investigated its crystal structure, band gap, thermal stability, and preliminary optical properties, alongside DFT calculations to compare experimental and theoretical results. Single-crystal XRD analysis confirmed the formation of 1D $[BiBr_4]^-$ anionic chains *via* edge-sharing $BiBr_6$ octahedra, revealing a well-ordered inorganic framework.

In this study, our primary focus is on the structural characteristics of the compound, which are examined through single-crystal X-ray diffraction (SCXRD) and interaction studies (using Hirshfeld surface analysis and DFT calculations), as well as the structural representations themselves. Vibrational spectroscopy and NMR are employed primarily to confirm the compound's molecular configuration.

Furthermore, we incorporate thermal analysis to assess the compound's stability, providing insights into its potential applications in the future, especially if thermal resistance becomes a critical factor. However, the main property investigated in this work is the optical behavior, with photoluminescence (PL) and diffuse reflectance spectroscopy (DRS) providing key data on its optical performance.

2. Experimental

2.1. Materials and characterization techniques

The title hybrid compound was created using commercially obtained chemical reagents $BiBr_3$ and HI, along with a non-commercial organic molecule 5-Amino-3-ethyl-1-phenyl-1*H*-1,2,4-triazole ($C_{10}H_{12}N_4$). No further purification was performed on these reagents. To study and obtain detailed compositional information on the crystal structure, we conducted vibrational studies using a PerkinElmer FT-IR Paragon 1000 PC spectrometer at room temperature to record the Fourier transform infrared (FT-IR) absorption, in the range of 4000–500 cm^{-1}. Additionally, we conducted Raman scattering using a Horiba/Jobin-6 Yvon T6400 spectrometer at room temperature, in the range of 4000–50 cm^{-1}.

The optical properties of the compound were examined using UV-vis spectroscopy in both solid and liquid states. Diffuse reflectance spectroscopy (DRS) was recorded at room temperature using a PerkinElmer Lambda 35 UV-vis spectrophotometer with an integrating sphere. A 6 mm pellet was used to obtain the spectrum over the 200–1100 nm range. For the liquid-state UV-vis spectrum, measurements were taken in a water solvent using a Cary 5000 UV-vis-NIR spectrophotometer, covering 250–600 nm. Additionally, photoluminescence (PL) spectra were acquired at room temperature in the same aqueous medium using a PerkinElmer LS 55 spectrometer, allowing the identification of emission maxima and evaluation of the radiative recombination characteristics. To further assess the energy gap and determine the nature of the electronic transition (direct or indirect), a correlation between solid- and liquid-state UV-vis spectra was established, complemented by TD-DFT analysis for both states.

2.2. Synthesis of $(C_{10}H_{13}N_4)[BiBr_4]\cdot 2H_2O$

A newly synthesized hybrid material (5-amino-3-ethyl-1-phenyl-1*H*-1,2,4-triazolium) tetrabromobismuthate(III) dihydrate with the formula $(C_{10}H_{13}N_4)[BiBr_4]\cdot 2H_2O$ was obtained through the slow evaporation synthesis method under ambient conditions (approximately 30 °C). The synthesis involved dissolving the organic molecule ($C_{10}H_{12}N_4$) and $BiBr_3$ (98% purity) separately in distilled water in a 1 : 1 molar ratio, with each solution stirred for approximately 30 minutes to ensure homogeneity. The two solutions were then combined, and concentrated hydrobromic acid (HBr, 48% purity) was added dropwise in three equal portions at half-hour intervals, with continuous stirring. After the final addition, the mixture was stirred for an additional 30 minutes, resulting in a total stirring time of 1.5 hours.

The solution was allowed to slowly evaporate over four days, leading to the formation of consistent, orange prismatic crystals. The crystals were isolated by filtration, and a single crystal, suitable for structural analysis, was carefully selected and examined using monocrystal X-ray diffraction. The synthesis was highly reproducible, with no observed challenges or variations. The resulting compound was found to be inherently stable under standard conditions, requiring no special storage considerations.

2.3. Single-crystal X-ray data collection and structure determination

The $(C_{10}H_{13}N_4)[BiBr_4]\cdot 2H_2O$ crystal structure was analyzed using Monocrystal X-ray Diffraction analysis at 293 K temperature. The analysis was performed with Mo–Ka radiation (I = 0.71073 Å) and XtaLAB Synergy, Dualflex, HyPix diffractometer on a selected crystal with dimensions of 0.15 × 0.15 × 0.04 mm^3. To analyze the crystallographic data, the Olex2-1.5 (ref. 30) software package was used. The structure was solved using direct methods and subsequently refined employing a full-matrix least squares approach on F^2, respectively, using SHELXT 2018/2 (ref. 31) and SHELXL 2018/3.[32] All non-hydrogen atoms were refined anisotropically, ensuring precise determination of their positional and thermal parameters. In contrast to the use of riding models, all hydrogen atoms were located directly from the Fourier difference maps and subsequently refined isotropically without geometrical constraints. The highquality diffraction data enabled the clear identification of every hydrogen position, including those belonging to the organic cation and the water molecules, ensuring a fully resolved and experimentally supported hydrogen-bonding network. The DIAMOND 3 software[33] was employed for generating crystal structure projections and visualizing packing interactions. Following iterative refinement cycles, the achieved final R_1 and wR_2 values were 0.023 and 0.0507, respectively. Detailed refinement conditions and structural resolution specifics for our compound are presented in Table 1.

2.4. Hirshfeld surface analysis

The Hirshfeld surface analysis technique[34–37] was utilized to identify, examine, and visualize different types of non-covalent contacts[38,39] between molecules, including hydrogen bonding, π–π stacking, and halogen interactions. This method partitions the electron density of the crystal into molecular fragments, facilitating a detailed exploration of intermolecular contacts. The structural data, provided in CIF format, were processed using CrystalExplorer 21.5 software[40] to generate Hirshfeld surfaces and corresponding 2D fingerprints,[41,42] which illustrate the relative contributions of different interaction types.

Each point on the Hirshfeld isosurface is characterized by two key distances: d_i, representing the distance from the surface to the closest atomic nucleus within the molecular boundary, and d_e, denoting the distance to the nearest nucleus outside the surface. The normalized contact distance, d_{norm}, is determined as the sum of the normalized values of d_i and d_e, as expressed by the following equations:

$$d_{\text{norm}} = \frac{d_i - r_i^{\text{vdw}}}{r_i^{\text{vdw}}} + \frac{d_e - r_e^{\text{vdw}}}{r_e^{\text{vdw}}}$$

where r_i^{vdw} and r_e^{vdw} are the atoms' van der Waals radii.[43,44]

2.5. Thermal analysis

Thermogravimetric (TG) analysis was carried out to evaluate the thermal stability of the hybrid material and its decomposition mechanism. The TGA analysis was performed using a 92 SETA RAM multi-module analyzer under a nitrogen atmosphere (N_2). The analysis was conducted at a constant heating rate of 10 °C per minute, starting from room temperature and continuing up to 500 °C, on 5.763 mg of the sample.

2.6. NMR (^{1}H and ^{13}C) spectroscopy

All NMR spectra were recorded using a Bruker AV400 Avance spectrometer (at 400 MHz for ^{1}H and 100 MHz for ^{13}C). Chemical shifts are expressed in parts per million (ppm) using TMS as an internal standard in DMSO.

2.7. Computational details

The structural, electronic, and optical properties of the hybrid $(C_{10}H_{13}N_4)[BiBr_4]\cdot 2H_2O$ were investigated through geometry optimization, vibrational frequency calculations, and HOMO–LUMO and Energy gap calculations, within the framework of

Table 1 Summary of crystal data and structure refinement details

Crystallographic data	
Empirical formula	$(C_{10}H_{13}N_4)[BiBr_4]\cdot 2H_2O$
Color/shape	Orange/Prism
Mass molar (g mol^{-1})	753.89
Diffractometer	XtaLAB synergy, Dualflex, HyPix diffractometer
Radiation type	Mo Kα (0.71073 Å)
Absorption correction	Multi-scan
Crystal system	Monoclinic
Space group	$P2_1/n$
Z/Z'	4/1
Unit cell parameters	
a (Å)	10.2869 (2)
b (Å)	7.3842 (2)
c (Å)	24.8911 (5)
β (°)	95.917 (2)
Absorption coefficient (mm^{-1})	17.88
Crystal size [mm]^3	0.15 × 0.15 × 0.04
Number of reflections measured variation of h, k, l	$h = -12 \rightarrow 12$, $k = -7 \rightarrow 10$, $l = -34 \rightarrow 32$
Scanning range of θ(°)	$2.9 < \theta < 30.2$
Number of measured, independent, and observed $[I > 2\sigma(I)]$ reflections	15853/4581/4099
F(000)	1376
Independent parameters	198
$\Delta\rho_{max}/\Delta\rho_{min}$ (e Å^{-3})	1.14/−1.34
$(\Delta/\sigma)_{max}$	< 0.003
$R[F^2 > 2\sigma(F^2)] = R_1$	0.023
$wR(F^2) = wR_2$	0.051
S = GooF	1.05
CCDC	2387887

density functional theory (DFT). All computations were carried out using the B3LYP functional[45] in Gaussian 09W,[46] with the GENECP keyword enabling a basis-set-mixing approach. The LANL2DZ[47] effective core potential (ECP) was applied to Bromine and bismuth to treat relativistic effects efficiently, while the 6–311++G* basis set was used for H, C, N, and O atoms to provide an all-electron, diffuse, and polarized description of the light-element orbitals. This combination ensures a balanced and physically meaningful treatment of both heavy and light atoms without excessive computational cost.

A molecular-cluster model, composed of one $[BiBr_4]^-$ anion, one organic cation, and two water molecules, was fully optimized with all atomic parameters relaxed to the minimum-energy configuration. This local model was adopted because periodic DFT calculations of the infinite one-dimensional $[BiBr_4]_n^{n-}$ chains would require a much larger computational domain and complex dispersion corrections to capture the long-range hydrogen-bonding and π–π stacking interactions. Such calculations are not computationally feasible at the hybrid-functional level. Nevertheless, the chosen cluster reproduces the local coordination geometry around Bi(III), the electronic distribution within the Bi–Br framework, and the cation–anion interactions with sufficient accuracy to interpret the experimental data reliably.

Vibrational frequencies were computed and compared with the experimental IR and Raman spectra, confirming the structural stability of the optimized model. GaussView 6.0.16 (ref. 48) was utilized to visualize and attribute the vibrational modes. Electronic descriptors, including the density of states (DOS), electron localization function (ELF), localized orbital locator (LOL), non-covalent interaction index (NCI-RDG), and electrostatic potential (ESP), were analyzed using Multiwfn.[49] This computational protocol provides a consistent and cost-effective description of the local electronic and optical behavior of the hybrid system.

3. Results and discussion

3.1. Crystal structure

Understanding a new hybrid material's properties and potential applications requires a detailed and comprehensive description of its crystal structure. We have synthesized a novel 1D bromobismuthate(III)-based organic-inorganic hybrid material, $(C_{10}H_{13}N_4)[BiBr_4]\cdot 2H_2O$, with a crystal structure that belongs to the first setting monoclinic crystal system. The new hybrid material is found in the centrosymmetric space group $P2_1/n$, meaning it represents the following symmetry operations: identity, inversion, an order 2 helical axis of rotation parallel to the *b*-axis, and a diagonal glide plane *n* perpendicular to the *b*-axis. The crystal system is a primitive monoclinic unit cell. No symmetry operation was found to pass through any of its entities, making the asymmetric unit the same as the formula unit ($Z' = 1$). This compound contains four formula units in its unit cell ($Z = 4$), based on the four determined symmetry elements in the crystal lattice and the Z′ value equal to one. The lattice parameters for this compound are: $a = 10.2869(2)$ Å, $b = 7.3842(2)$ Å, $c = 24.8911(5)$ Å, and $\beta = 95.917(2)°$. Fig. 1(a) shows a presentation of the formula unit using DIAMOND 3, which consists of one monoprotonated organic cation $(C_{10}H_{13}N_4)^+$, one tetrahedral $[BiBr_4]^-$ of the 1D chain of $[BiBr_4]_n^{n-}$ inorganic entity, and two H_2O molecules sitting between the organic cation and the inorganic entities. The crystal structure does not show any disordered atoms or defects, such as impurities. This indicates that the structure is stable, as evidenced by the normal ellipsoid volume of the atoms (Fig. 1(a)), showing no disorder or excess electron density. Table 1 provides a comprehensive summary of the lattice parameters, unit cell volume, and key crystallographic characteristics of the newly synthesized crystal structure. Additionally, Table 1.S presents the atomic coordinates along with their respective equivalent isotropic displacement parameters (U_{eq}).

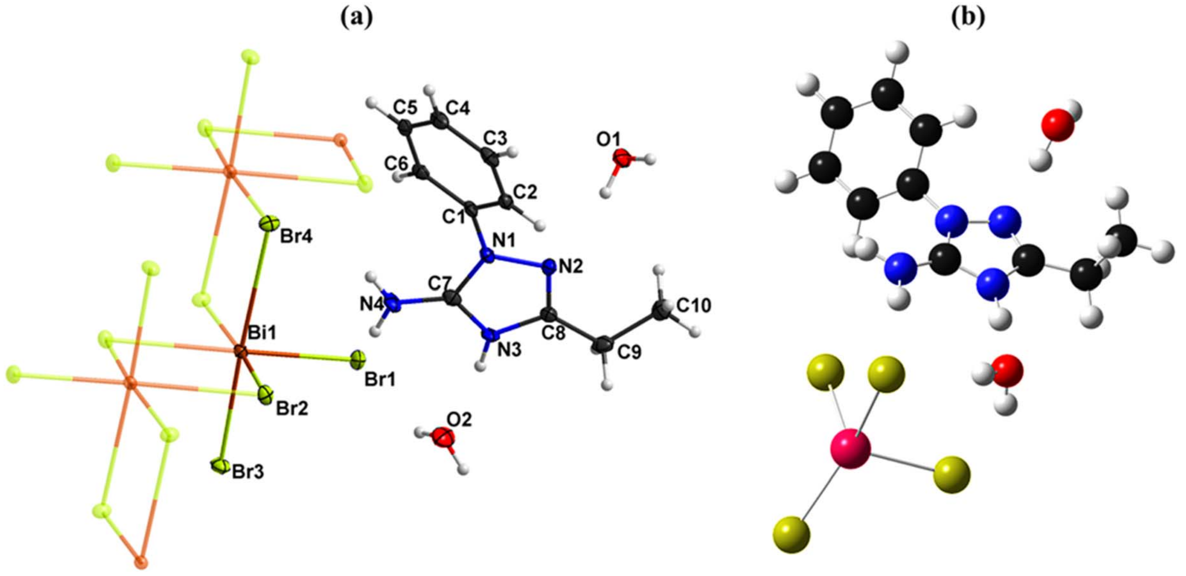

Fig. 1 (a) The formula unit and (b) the optimized geometry of the title compound.

Fig. 1(b) illustrates the optimized molecular geometry of the hybrid compound. A comparative analysis reveals that the majority of the optimized bond distances are slightly longer than their experimentally determined counterparts. This discrepancy is anticipated, as theoretical calculations are performed on an isolated molecule in the gas phase, whereas experimental measurements reflect a solid-state environment influenced by intermolecular interactions and crystal packing effects. These results validate the selected computational model and methodology, confirming the reliability of the calculations. Consequently, the choice of DFT calculation level of theory is deemed suitable for accurately describing the structural characteristics of the complex.

Fig. 2 provides valuable insights into the crystal structure. The projection along the *a*-axis, for instance, reveals that the inorganic entities are arranged in a one-dimensional chain of octahedral polyhedra, represented as $[\mathrm{BiBr_4}]_n^{\,n-}$. These anionic entities exhibit one-dimensional structural association types along the *b*-axis. The anionic chains occupy two positions in the unit cell along the *a*-axis; one in the corner and the other passing through the center of the unit cell. Notably, the stabilization of these anionic chains is facilitated by the surrounding water molecules, which interact with the polyhedral units, reinforcing the structural integrity of the framework, which can be seen more clearly in Fig. 1.S.

The organic molecule's coordination environments consist of four nearest neighbors, 1D inorganic chains. Fig. 3 highlights notable variations in Bi–Br bond lengths, ranging from 2.6812(4) Å to 3.1803(4) Å. The Br–Bi–Br bond angles fall within 83.496(11)° to 96.503(11)° for cis configurations and 172.061(12)° to 177.061(12)° for trans configurations. The most pronounced disparity in Bi–Br bond lengths, measuring 0.499 Å, occurs between two opposing halogen atoms (Bi–Br1, Bi1–Br2ii). A detailed overview of the geometric parameters, including bond lengths and angles within the anionic units, is provided in Table 2.S. The observed bond length variations and bond angle deviations introduce slight distortions in the $\mathrm{BiBr_6}$ octahedron ($\mathrm{ID(Bi{-}Br)} = 10^{-4}$). These distortions can be attributed to both primary deformations, governed by the stereochemical activity of Bi's lone electron pair, and secondary deformations arising from hydrogen bonding interactions.

$$\mathrm{ID(Bi-Br)} = \frac{1}{6}\sum_{1}^{6}\left|\frac{\mathrm{BiBri} - \ \mathrm{BiBrm}}{\mathrm{BiBrm}}\right| = 10^{-4}$$

where the variables BiBri($i = 1$ to 6) represent the individual Bi–Br bond lengths, and BiBrm denotes the mean bond length within the distorted octahedral unit.

The arrangement of atoms or ions within a crystal lattice can affect the properties of a material, such as its mechanical strength and thermal conductivity. There are two methods to evaluate the efficiency of this arrangement: direct and indirect. The density of a crystal is a direct measure of how efficiently its atoms or ions are packed, with higher densities indicating better packing efficiency. Our hybrid material has a density of 2.663 g cm^{-3}, which is considered high and indicates good packing efficiency. Void analysis is another method to determine the efficiency of packing by assessing the presence of empty spaces or pores within the crystal structure. Void analysis can impact packing efficiency and the overall properties of the material. As part of the Hirshfeld analysis, we conducted a crystal void analysis to determine the packing efficiency of the

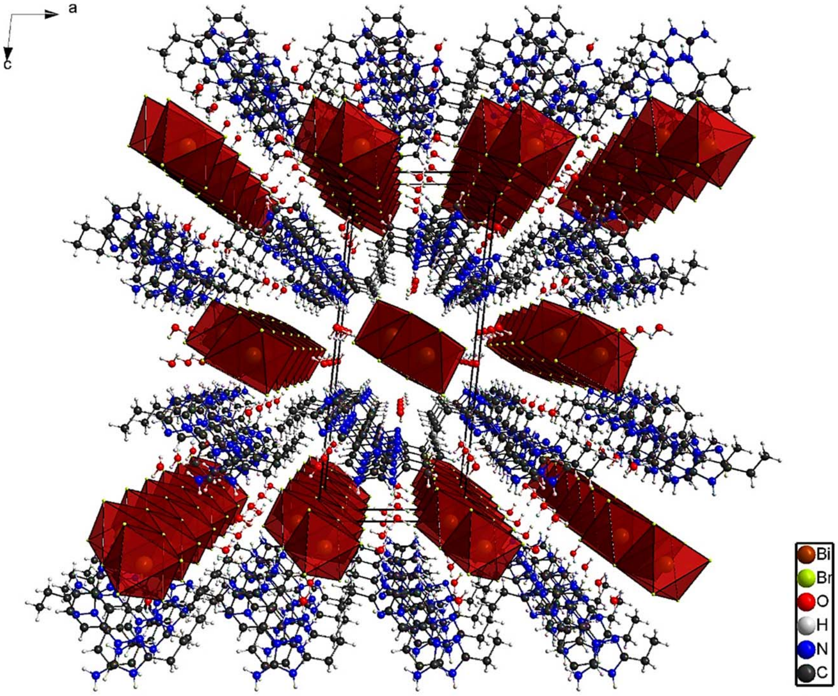

Fig. 2 Projection along the *b*-axis for the arrangement of the 1D inorganic chains.

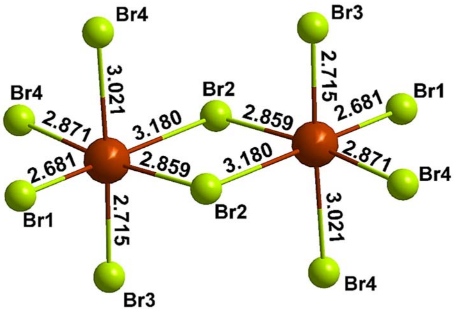

Fig. 3 Variations in Bi–Br bond lengths within the octahedral geometry.

crystal structure. We arrived at the same conclusion as the direct method.

Fig. 1.S shows the arrangement of four organic molecules parallel to the (c,a) plane within the unit cell. Each cation is monoprotonated at N_3, occupying positions ($x = 3/4$, $x = 1/4$) and ($x = 1/4$, $z = 3/4$). The protonation site, initially indicated by X-ray diffraction, was confirmed by DFT and ^1H NMR. Charge distribution analysis identified N3 as the most basic site, and optimization of alternative protonation models confirmed that the experimental structure corresponds to the most stable configuration. Validation by ^1H NMR is discussed separately. Table 3.S reports the main geometrical parameters of the organic groups. Bonding in the crystal is categorized into five types: covalent bonds within the cations, Bi–Br metal–halogen bonds in the anions, and ionic, hydrogen, and π-stacking interactions linking the organic and inorganic components.

The selection of the non-commercial organic cation $(C_{10}H_{13}N_4)^+$ plays a critical role in stabilizing the low-dimensional inorganic framework and modulating the resulting physical properties. Unlike commonly employed commercial ammonium or alkylammonium cations, this heterocyclic cation has been specifically designed and previously employed in our earlier studies, where it demonstrated a strong ability to promote structural order, hydrogen-bonding networks, and enhanced framework stability in bismuth-based hybrid materials. The presence of multiple nitrogen donor sites facilitates robust hydrogen bonding with halide ligands and lattice water molecules, contributing to the formation of well-defined one-dimensional architectures and suppressing structural disorder. These features are known to influence carrier localization, phonon coupling, and optical absorption behavior, thereby indirectly governing the electronic and optoelectronic properties observed in the present compound.

The structure is reinforced by an extended hydrogen-bond network composed of O–H⋯Br, O–H⋯N, and N–H⋯O interactions, forming five distinct hydrogen bonds. Interstitial water molecules bridge organic cations and nitrogen atoms, generating a two-dimensional network that enhances cohesion. According to Brown's criterion,[50] O_1–H_{1A}⋯$Br_{3(iii)}$ and O_2–H_{2B}⋯Br_1 correspond to weak hydrogen bonds ($d_{D-A} > 3.19$ Å). Blessing's criterion[51] distinguishes strong from weak O–H⋯N and N–H⋯O bonds at $d_{D-A} = 2.7$ Å; thus, N_3–H_3⋯O_2 is classified as strong, while O_1–H_{1B}⋯N_2 and N4–H_{4B}⋯$O_{1(iv)}$ are weak. Fig. 2.S illustrates the arrangement of these hydrogen bonds in the asymmetric unit and unit cell, with bond distances and angles summarized in Table 2.

Table 2 Interatomic distances and hydrogen bond angles of the compound[a]

D—H⋯A	D—H (Å)	H⋯A (Å)	D⋯A (Å)	D—H⋯A (°)
O_1–H1A⋯$Br_3{}^{iii}$	0.85	2.59	3.364 (3)	152
O_1–H1B⋯N_2	0.85	2.05	2.888 (4)	167
O_2–H2B⋯Br1	0.85	2.68	3.442 (3)	151
N_3–H_3⋯O_2	0.86	1.86	2.688 (4)	162

[a] Symmetry codes : (iii) $x + 1/2, -y + 1/2, z - 1/2$; (iv) $-x + 3/2, y + 1/2, -z + 1/2$.

Beyond hydrogen bonding, π-stacking interactions contribute significantly to lattice stability. As shown in Fig. 6, three types are observed: π–π stacking (3.652 Å, red), N–H⋯π (3.341 Å, green), and C–H⋯π (3.668 Å, violet). These values fall within the accepted ranges (π–π: 3.4–4.0 Å; N–H⋯π: 2.5–4.0 Å; C–H⋯π: 3.3–4.0 Å). The interactions occur between benzene ring centroids, amine groups, and para-position hydrogens, stabilizing parallel organic molecules along the *b*-axis in alignment with the 1D inorganic chain (Fig. 3.S). Collectively, the hydrogen-bonding and π-stacking networks ensure strong cohesion and robust lattice stability.

3.2. Vibrational studies

FTIR spectroscopy and Raman scattering at room temperature were used to analyze the functional groups and clarify the crystal structure. In the FTIR analysis, the focus was on the vibrations of the organic cation, as the vibrations of the inorganic anion could not be detected due to its significant mass. Raman scattering was used to identify the vibrational modes of the anionic component. Theoretical calculations using Density Functional Theory (DFT) were used to accurately assign the observed spectral bands. Fig. 4 shows the visual comparison between the experimental and theoretical FTIR absorption spectra, while Fig. 5 presents the experimental and theoretical Raman spectra of $(C_{10}H_{13}N_4)[BiBr_4]\cdot 2H_2O$. Table 4.S presents a detailed comparison of the experimentally observed and theoretically calculated vibrational modes of the hybrid compound, revealing a strong correlation between the two sets of wavenumbers. The close agreement between the experimental and computational results validates the proposed mode assignments. Although periodic calculations offer a more precise representation of the system, their implementation is considerably time-intensive.

3.3. $[BiBr_4]_n^-$ anionic chain vibrational modes

The Raman spectrum of $(C_{10}H_{13}N_4)[BiBr_4]\cdot 2H_2O$ exhibits several well-defined bands characteristic of the one-dimensional $[BiBr_4]_n^{n-}$ chain, in which individual seesaw-shaped $[BiBr_4]^-$ units are interconnected through bridging bromide

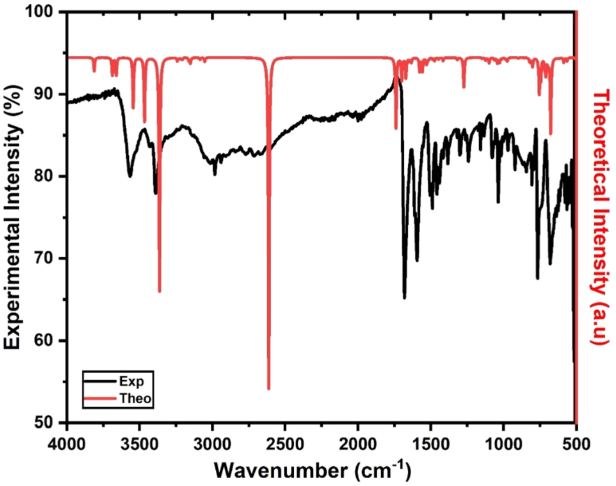

Fig. 4 FT-IR spectrum of the title compound.

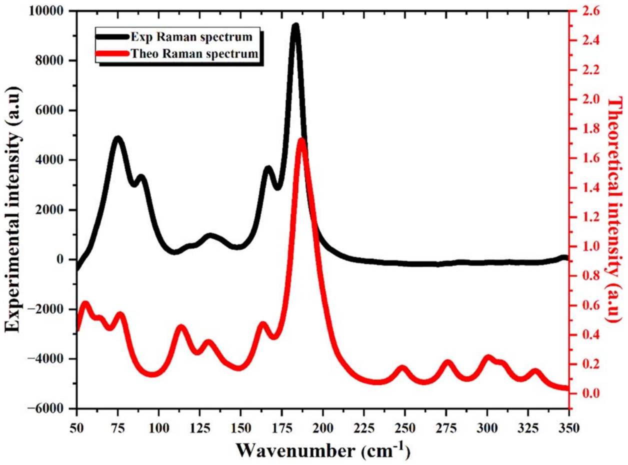

Fig. 5 Raman spectrum of the title compound.

atoms to form distorted $BiBr_6$ octahedra. The most intense features are observed in the low-frequency region (50–200 cm^{-1}), typical of Bi–Br lattice vibrations. Distinct experimental peaks appear at 183, 166, 131, 118, 90, and 75 cm^{-1}, which align closely with the calculated values of 186, 164, 131, 113, 84, and 68 cm^{-1}, respectively. These modes can be attributed as follows: the bands at 183 and 166 cm^{-1} correspond to the asymmetric and symmetric stretching vibrations of terminal Bi–Br bonds within distorted octahedra; the band at 131 cm^{-1} arises from mixed bridging and terminal Bi–Br deformations; the peaks at 118 and 90 cm^{-1} are due to bridging Bi–Br bending and torsional motions; and the low-frequency feature at 75 cm^{-1} originates from collective lattice translations along the $[BiBr_4]_n^{n-}$ chain. The excellent agreement between experimental and theoretical wavenumbers confirms the reliability of the computational model and reflects the strong structural correlation between the localized Bi–Br dynamics and the extended octahedral chain architecture of the hybrid compound.

3.4. $(C_{10}H_{13}N_4)^+$ organic cations vibrational modes

The newly synthesized hybrid compound features an organic cation and H_2O molecules, both of which participate in various bonding interactions that are detectable in IR and Raman spectra, exhibiting distinct frequency ranges and intensities. The IR spectrum is divided into two primary regions: the functional group region and the fingerprint region. The functional group region encompasses symmetric and asymmetric stretching vibrations of aromatic C–H bonds, ethyl C–H bonds, N–H bonds, and O–H bonds from water molecules. Notably, the highest-frequency peak at 3814 cm^{-1} corresponds to the asymmetric stretching vibration of one of the two H_2O molecules in the structure, aligning closely with the theoretically predicted value of 3811 cm^{-1}. The band at 3736 cm^{-1} is attributed to the asymmetric stretching of NH_2, with a computed value of 3687 cm^{-1}. The second H_2O molecule has an asymmetric stretching vibrational mode at 3665 cm^{-1}, with a theoretical frequency of 3660 cm^{-1}. The symmetric stretching vibrations of both H_2O molecules are located at 3558 and 3433 cm^{-1}, with theoretical frequencies of 3544 and 3466 cm^{-1}, respectively. The symmetric vibrational mode of the NH_2 bond is observed at 3392 cm^{-1} and theoretically at 3363 cm^{-1}. The symmetric stretching vibration of benzene C–H bonds is observed experimentally and theoretically at 3262 and 3240 cm^{-1}, respectively. The asymmetric and symmetric stretching vibrational modes of CH_2 and CH_3 (ethyl group) bonds are observed at 3142, 3058, and 3022 cm^{-1}, with theoretical frequencies of 3161, 3086, and 3053 cm^{-1}, respectively. The N–H⋯O hydrogen bonds exhibit a stretching vibrational mode at 2663 cm^{-1}, theoretically assigned at 2613 cm^{-1}. In the fingerprint region, additional bands are observed, including various vibrational bending modes of light bonds such as N–H, NH_2, C–H, CH_3, and H_2O bonds. Heavier bonds, such as C=C, C–N, C–C, and C–C=C, also present stretching vibrational modes in this region.

3.5. Thermogravimetric analysis

The thermal stability and decomposition mechanisms of the hybrid material were investigated by thermogravimetric analysis (TGA) (Fig. 6). A 5.763 mg sample was heated from 30 to 500 °C at 10 °C min^{-1} under nitrogen flow (20 mL min^{-1}). The inert atmosphere was chosen to follow dehydration, desorption, and decomposition under non-oxidative conditions, avoiding interference from oxidation. The compound in its anhydrous phase exhibits good stability up to ∼275 °C, after release of structural water, in line with the 200–300 °C range generally reported for poor-metal hybrid materials employed in optoelectronics.

3.5.1. The TGA/DTG curves show two main weight-loss events. The first weight loss, at ∼135 °C, corresponds to the removal of two structural water molecules (experimental 4.26% *vs.* theoretical 4.76%, error 0.5%), and reflects a dehydration process rather than chemical degradation. This transition marks the conversion of the hydrated phase into an anhydrous form, while preserving the integrity of the inorganic $[BiBr_4]_n^{n-}$ framework and the organic cation. No additional mass loss or

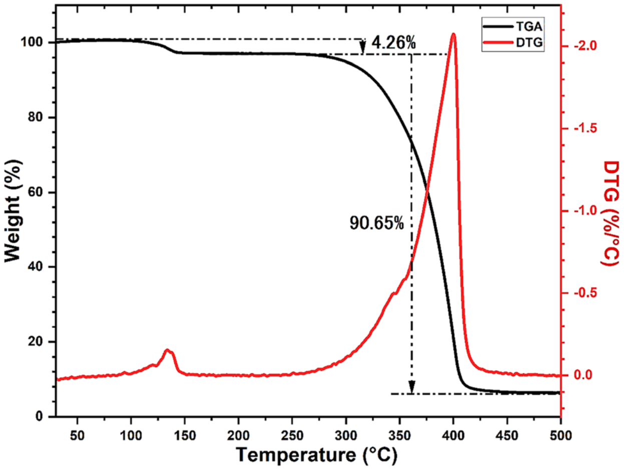

Fig. 6 TGA thermal analysis curve of the $(C_{10}H_{13}N_4)[BiBr_4]\cdot 2H_2O$ compound.

structural collapse is detected until approximately above 275 °C, indicating that the anhydrous phase remains thermally stable over a wide temperature range. Therefore, the compound exhibits phase-dependent thermal stability, with the hydrated form stable up to ~100–135 °C and the anhydrous framework maintaining structural integrity up to ~275 °C.

The second weight loss, occurring between 300 and 450 °C with a maximum at 400 °C (90.65% weight loss), reflects the decomposition of the organic cation and the collapse of the $[BiBr_4]_n^{n-}$ chains. Unlike transition-metal hybrids, poor-metal-based anionic complexes typically cannot withstand temperatures above 450 °C. The presence of a single sharp decomposition peak highlights the high homogeneity of the material, which decomposes uniformly and leaves only solid carbonaceous residues.

3.6. NMR (^{1}H and ^{13}C) spectroscopy

3.6.1. ^{1}H NMR. According to the spectral analysis of the protons, as seen in Fig. 4.S, we see that compared to 5-amino-3-ethyl-1-phenyl-1*H*-1,2,4-triazole taken as an organic cation, the shift of the signal of the NH_2 group of 6.33 to 8.24 in the compound indicates protonation occurs on this amino group. Fig. 5.S shows the result of ^{13}C NMR for more clarification. Note that the numbering in Scheme 1 is not the same as in the formula unit in Fig. 1.

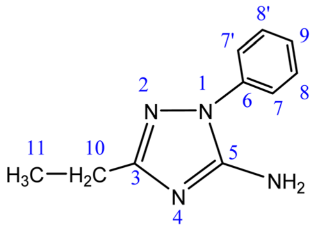

Scheme 1 Molecular structure of the organic cation and hydrogen atoms positions.

NMR ^{1}H: (400 MHz, DMSO-d$_6$) [ppm] δ = [H11] 1.24 (t, 3H, *J* = 7.5 Hz) [H10] 2.67 (q, 2H, *J* = 7.5 Hz) 7.55–7.63 (*m*, 5H) [H7, H7′, H8, H8′, H9], 8.24 [NH_2].

NMR ^{13}C: (100 MHz, DMSO-d$_6$) [ppm]δ = [C3] 153.53, [C5] 150.04 [C6] 135.12, [C8, C8′] 130.29 [C9] 129.82, [C7, C7′] 125.18 [C10] 19.44 [C11] 11.16.

3.7. Optical study

3.7.1. UV-vis spectroscopy and photoluminescence properties. The optical properties of $(C_{10}H_{13}N_4)[BiBr_4]\cdot 2H_2O$ were investigated through liquid-state UV-vis absorption, steady-state photoluminescence (PL) emission, and solid-state diffuse reflectance spectroscopy (DRS) to assess its semiconducting behavior and electronic transitions. The UV-vis spectrum in aqueous solution (Fig. 7) revealed distinct absorption features corresponding to electronic transitions within the $[BiBr_4]_n^{n-}$ chain.

To evaluate the semiconducting nature of the material and its energy gap, the optical band gap was determined using the Tauc formalism,[52] where a linear fit of the absorption edge in the $(\alpha h\nu)^n$ *vs.* $h\nu$ plot was used to compare and distinguish between direct and indirect transitions. Comparison of the direct and indirect Tauc representations, shown in Fig. 8, along with the photoluminescence (PL) emission plot (Fig. 9), indicated that the material follows the indirect transition model (n = 2) and possessed an indirect energy gap (E_{gind}) of 2.77 eV in the liquid state, consistent with the theoretical predictions for Bi-based hybrids characterized by strong spin–orbit coupling and structural distortion. This correlation between UV-vis, PL, and DRS data confirms that $(C_{10}H_{13}N_4)[BiBr_4]\cdot 2H_2O$ exhibits an indirect band structure, characteristic of its one-dimensional Bi–Br framework. These results collectively demonstrate that the compound behaves as a wide-band-gap semiconductor, further substantiated by DRS measurements discussed in the following section.

Photoluminescence (PL) spectroscopy, complemented by the CIE 1976 chromaticity diagram (U, V), provides critical insights

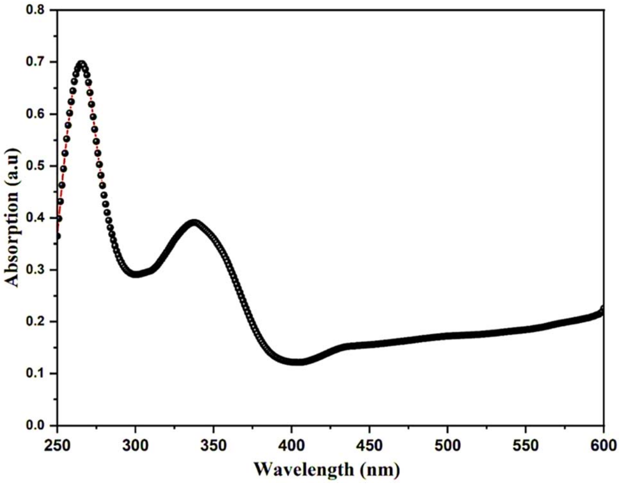

Fig. 7 UV-visible optical absorption.

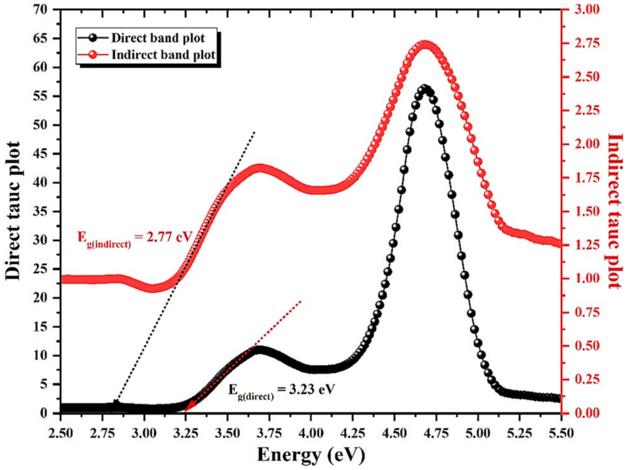

Fig. 8 Direct *vs.* indirect transitions Tauc plots.

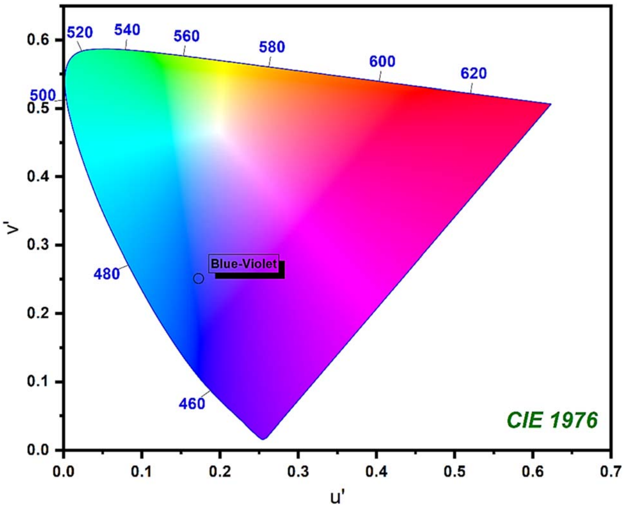

Fig. 10 Chromaticity diagram of $(C_{10}H_{13}N_4)[BiBr_4]\cdot 2H_2O$.

into the photophysical and colorimetric behavior of hybrid materials. PL analysis distinguishes excitation and emission processes: the excitation spectrum records the emission intensity as a function of excitation wavelength, while the emission spectrum maps the emitted light intensity over wavelength. In this work, steady-state PL measurements were conducted under continuous excitation, allowing the evaluation of optical emission behavior. Although time-resolved PL was not employed, the nature of the photoluminescence can still be logically inferred from experimental relationships between the emission maxima and the electronic transition energies. The observed emission maximum lies close to the optical absorption edge obtained from UV-vis and DRS measurements, indicating that the emission originates from direct electronic relaxation within the same energy manifold, a hallmark of fluorescence rather than phosphorescence, as phosphorescent emission typically occurs at substantially lower energies than the excitation energy.

The photoluminescence (PL) spectrum of $(C_{10}H_{13}N_4)[BiBr_4]\cdot 2H_2O$, recorded under excitation at 259 nm over the 250–800 nm spectral range, displays a broad and intense emission band centered at approximately 400 nm, extending across a wide portion of the visible region. This pronounced spectral broadening is indicative of phonon-assisted radiative recombination processes, which are characteristic of indirect band gap hybrid materials and are frequently associated with lattice relaxation and carrier localization effects in low-dimensional systems. The presence of an excitation band centered around 414 nm, corresponding to the maximum emission intensity (~95 a. u.), reflects an efficient photoluminescence response under optical excitation conditions, without implying dominance of direct band-to-band radiative recombination (Fig. 9).

Colorimetric evaluation using the CIE 1976 UCS (U, V) chromaticity diagram (Fig. 10) provides a perceptually uniform description of the emission characteristics. The calculated chromaticity coordinates (u′ = 0.1725, v′ = 0.2513) place the emission firmly within the blue–violet region of the visible spectrum, indicating high color purity and good chromatic

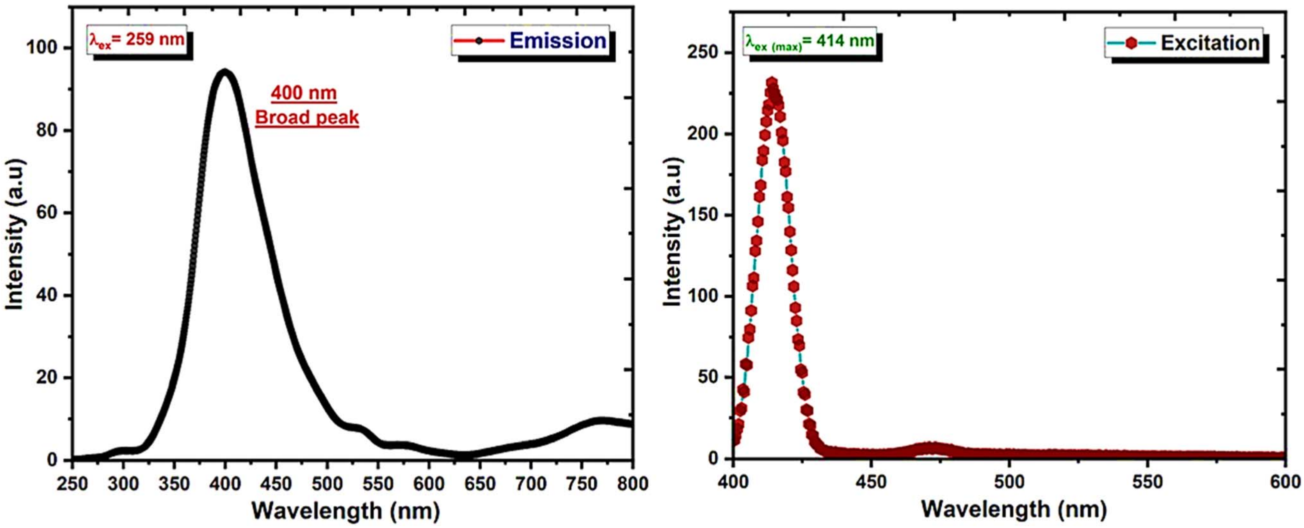

Fig. 9 Emission and excitation plots of photoluminescence.

stability under photoexcitation. Importantly, this colorimetric and photoluminescence analysis is intended to characterize the optical emission behavior of the material under optical excitation, rather than to suggest electroluminescent device performance. In this context, the observed emission properties are best regarded as relevant for photoluminescence-based photonic functionalities and for fundamental structure–property investigations of emission mechanisms in low-dimensional organic–inorganic halide frameworks, fully consistent with the indirect band-gap nature of the compound.

3.7.2. Diffuse reflectance spectroscopy (DRS). Optical spectroscopy provides fundamental insight into the electronic structure and band dynamics of semiconductors, allowing precise evaluation of their optical band gap (E_g) and transition nature (direct or indirect).[53,54] In the present study, a comprehensive optical investigation was carried out on $(C_{10}H_{13}N_4)[BiBr_4]\cdot 2H_2O$, integrating UV-vis diffuse reflectance spectroscopy (DRS), absorbance analysis, and a series of derived optical parameters including the Urbach energy, threshold wavelength, penetration depth, optical extinction coefficient, refractive index, and optical conductivity. The solid-state DRS spectrum was employed to determine E_g using the Kubelka–Munk (K–M) transformation, while the electronic band structure was cross-validated by DFT calculations (Fig. 18), ensuring consistency between experimental and theoretical findings.

The diffuse reflectance and absorbance spectra (Fig. 11(a) and (b)) reveal three principal absorption bands at 262 nm (4.73 eV), 332 nm (3.73 eV), and 396 nm (3.13 eV), comparable to those typically observed in bismuth-based organic–inorganic hybrid films.[55–60] These multiple absorptions are characteristic of halogenobismuthate(III) compounds, where transitions arise primarily from ligand-to-metal charge transfer (LMCT) processes.[61,62] The molecular orbital diagram for $[BiX_6]^{3-}$ (Fig. S7(a)) shows the highest occupied molecular orbital (HOMO) localized on the Bi(III) 6 s^2 orbitals and the lowest unoccupied molecular orbital (LUMO) on the Bi(III) 6p orbitals. Within the O_h symmetry framework (Fig. S7(b)), interaction between the np orbitals of the halide (t_1g, t_2g, t_1u, t_2u) and the Bi 6p (t_1u) orbitals gives rise to the LMCT transitions. Substitution of a more electronegative halogen (Cl) by a less electronegative one (I) systematically redshifts the absorption bands,[63–65] consistent with known halogen trends.

In this compound, the first absorption band at 262 nm is attributed to π–π* transitions within the organic cation, while the second band at 332 nm arises from LMCT transitions between bromide and Bi(III). The third absorption band at 396 nm corresponds to intra-framework charge transfer along the one-dimensional $[BiBr_4]_n^{n-}$ chain, which dominates the electronic transition behavior. The broad absorption tail extending from 500 to 700 nm in the DRS spectrum originates from phonon-assisted transitions, a hallmark of indirect band gap semiconductors. The strong agreement between experimental and theoretical absorption spectra (Fig. S6) further confirms the reliability of these assignments. The one-dimensional $[BiBr_4]_n$ framework and the presence of heavy Bi^{3+} centers promote strong light–matter interaction and carrier localization, which manifest as intense optical absorption, indirect band-gap behavior, and phonon-assisted relaxation processes. These features are particularly favorable for applications relying on light harvesting and photoresponse rather than radiative emission.

One-dimensional bismuth halide hybrids are widely known to favor indirect band gaps, mainly due to the strong spin–orbit coupling (SOC) associated with Bi(III). SOC induces band splitting and symmetry reduction near the Fermi level, promoting momentum-dependent (phonon-mediated) transitions characteristic of indirect semiconductors. This is corroborated by fitting the logarithmic Tauc relation, $\ln(\alpha h\nu) = \ln B + n\ln(h\nu - E_g)$, yielding $n = 2.08 \approx 2$, as illustrated in Fig. 12(b),

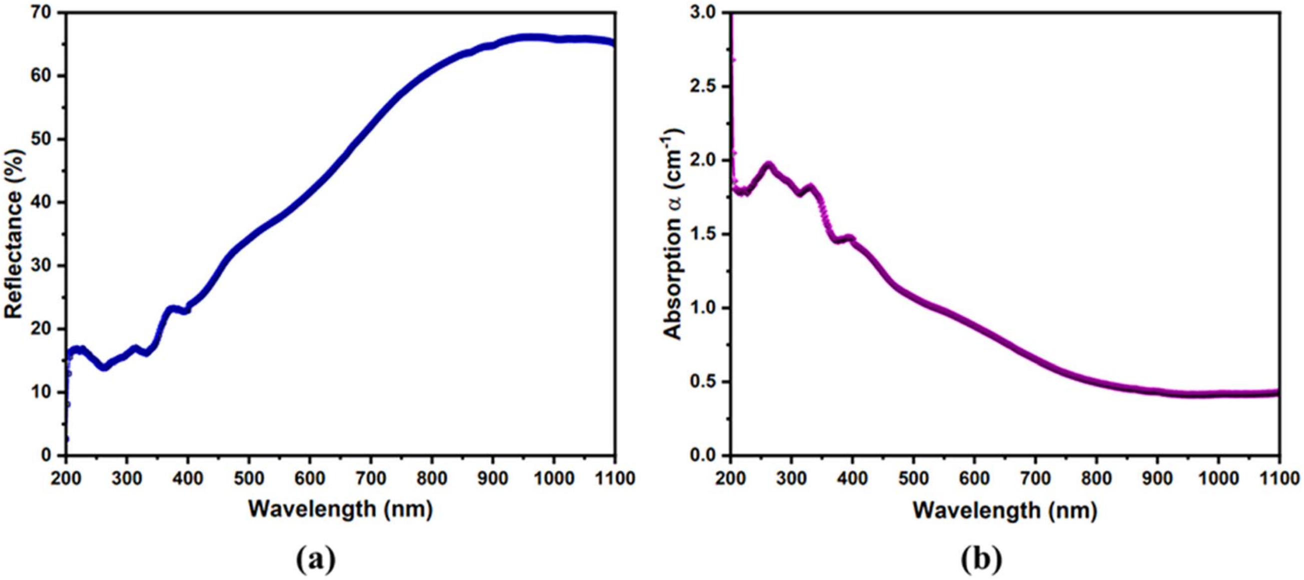

Fig. 11 (a) Diffuse reflectance and (b) absorption spectrum.

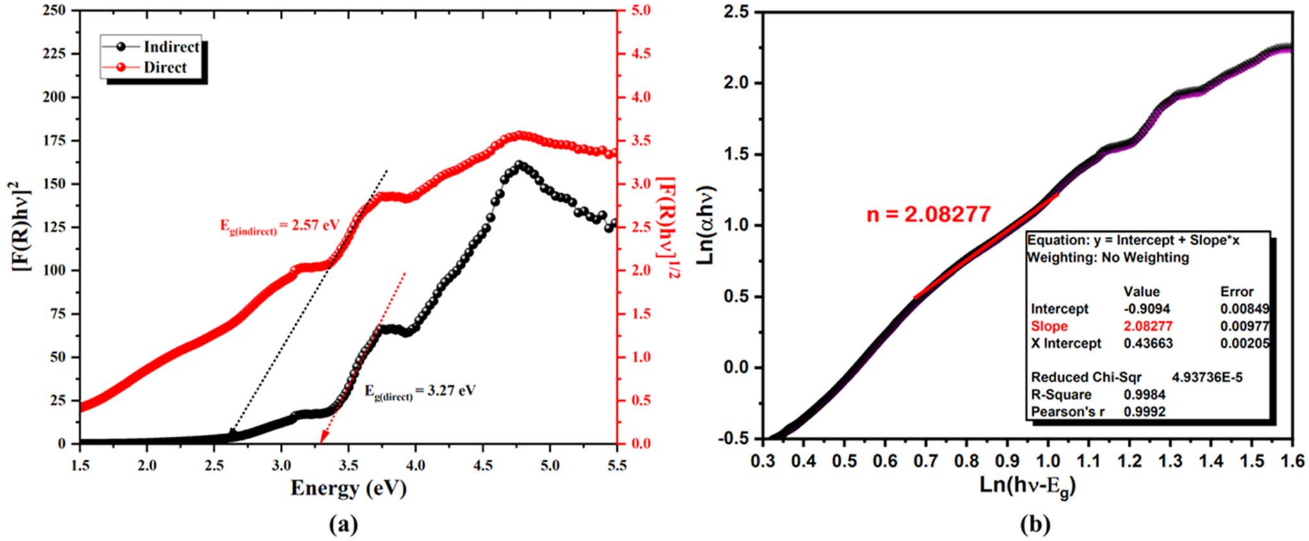

Fig. 12 (a) Direct *vs.* indirect band gap determination *via* Tauc plot, (b) validation of *n* value using the $L_n(\alpha h\nu)$ *vs.* $L_n(h\nu - E_g)$ Plot.

unambiguously confirming the indirect band gap nature of the compound.

The observed indirect band-gap character of $(C_{10}H_{13}N_4)[BiBr_4]\cdot 2H_2O$ can be rationalized by the combined effects of the heavy Bi^{3+} cation and the one-dimensional inorganic framework. The large atomic mass of bismuth induces strong spin–orbit coupling (SOC), which significantly perturbs the electronic band structure by lifting band degeneracies and redistributing the conduction and valence band extrema in momentum space. In low-dimensional bismuth halides, this SOC-driven band splitting frequently results in indirect electronic transitions, as reported for related Bi-based hybrid systems. The one-dimensional connectivity of the $[BiBr_4]_n$ chains further enhances carrier localization and reduces band dispersion, reinforcing phonon-assisted recombination pathways and favoring indirect-gap behavior. These structural and electronic characteristics collectively explain the experimentally observed indirect band gap, strong optical absorption, and broad photoluminescence response.

The absorption edge near 480 nm corresponds closely to the observed orange coloration of the crystals, further supporting an energy gap near 2.6 eV, as estimated by the less precise UV-vis method. The Kubelka–Munk theory, commonly applied to analyze DRS data from weakly absorbing powders, was used to refine the band gap estimation. The Kubelka–Munk function, defined as:[66,67]

$$F(R) = \frac{K}{S} = \frac{(1 - R_\infty)^2}{2R_\infty}$$

In this context, R represents the absolute reflectance of the sample, measured using an integrating sphere system. K is the light absorption coefficient, and S is the scattering coefficient. The function (R) is known as the Kubelka–Munk function. According to inter-band absorption theory, the absorption coefficient near the threshold, in relation to incident energy, can be described by the following equation:[68,69]

$$\left[\frac{F(R)h\nu}{t}\right]^{\frac{1}{n}} = A\left(h\nu - E_g\right)$$

The holder thickness, t, is 1 mm, and the constant A remains the same across all energies. The index n varies based on the type of optical transition: for direct band gaps, $n = 1/2$, and for indirect band gaps, $n = 2$. The plot of $[(R)h\nu/t]^{1/2}$ *versus* photon energy $h\nu$, shown in Fig. 12(a), is linear, indicating an indirect allowed transition. By linear extrapolation, the energy band gap for this transition is estimated at 2.57 eV, confirming the use of $n = 2$, and closely matching the 2.6 eV calculated *via* the Zero-DOS method (Fig. 18). Notably, the gap decreases with a lower X/Bi ratio, with the smallest gap at X/Bi = 4. Additionally, connectivity in $[BiX_6]$ octahedra affects the gap: edge-sharing $[BiX_6]$ chains exhibit the lowest gap, while mixed edge- and corner-sharing $[Bi_2X_9]$ chains have higher gaps. These findings highlight the need for further theoretical studies to fine-tune band gap properties.[70]

Determination of Urbach energy and threshold wavelength

Determining Urbach energy (E_U) and threshold wavelength is crucial for characterizing a compound. The Urbach energy provides valuable insight into the degree of structural disorder and quantifies the density of localized states near the band edges in semiconducting materials. It is derived from the exponential absorption tail in the low-energy region of the absorption spectrum by plotting $\ln(\alpha)$ (absorption coefficient) *versus* photon energy ($h\nu$) and extrapolating the linear segment based on the Urbach model.[71] A higher E_U indicates greater structural disorder, typically due to foreign atom incorporation, reducing the effective optical gap. The formula used is:

$$\mathrm{Ln}(\alpha) = \mathrm{Ln}\ (\alpha_0) + \frac{h\nu}{E_u}$$

where α is the absorption coefficient, $h\nu$ the photon energy, and E_u the Urbach energy. The slope of the linear region of the plot of $\ln(\alpha)$ *versus* $h\nu$ (Fig. 13) provides the numerical value of E_u.

For $(C_{10}H_{13}N_4)[BiBr_4]\cdot 2H_2O$, the calculated Urbach energy is 840 meV, corresponding to approximately 32.8% of the optical band gap. This relatively high value reflects the presence of tail states induced by lattice distortion and phonon-assisted transitions, typical of one-dimensional Bi–Br frameworks. The elevated E_u originates from the strong spin–orbit coupling (SOC) of Bi(III), which lowers symmetry and increases the density of localized electronic states near the band edges. Such effects are intrinsic to Bi-based halometallate hybrids and directly contribute to their indirect band gap behavior.

The threshold wavelength (λ_i), corresponding to the longest wavelength initiating significant absorption, was determined from the relation:[72,73]

$$\left(\frac{\alpha}{\lambda}\right)^2 = C\left(\frac{1}{\lambda} - \frac{1}{\lambda_i}\right)$$

where C is a proportionality constant. The extrapolation of the linear portion of the $(\alpha/\lambda)^2$ *versus* $1/\lambda$ curve (inset of Fig. 13) gives $\lambda_i = 583$ nm, marking the onset of photon absorption. This wavelength corresponds to the fundamental excitation threshold of the material, consistent with the band structure deduced from DRS and PL analyses.

Together, the high Urbach energy and the defined threshold wavelength confirm the presence of structural flexibility and phonon-coupled transitions within the $[BiBr_4]_n^{n-}$ chain, supporting the indirect semiconducting nature of the hybrid compound.

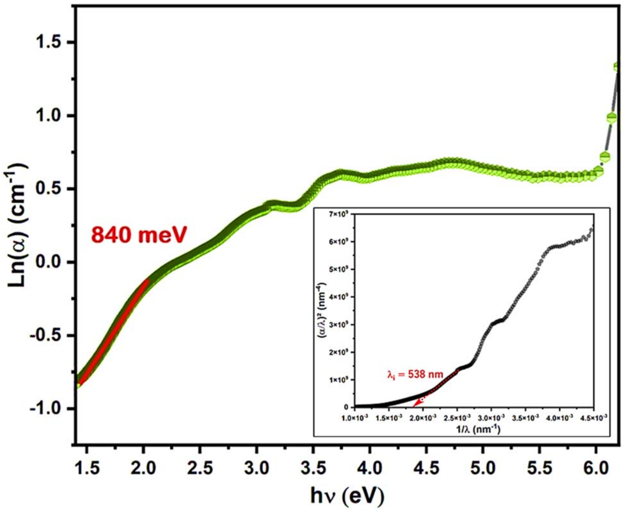

Fig. 13 Urbach energy analysis (the inset is the evolution of the $(\alpha/\lambda)^2$ curve as a function of $1/\lambda$).

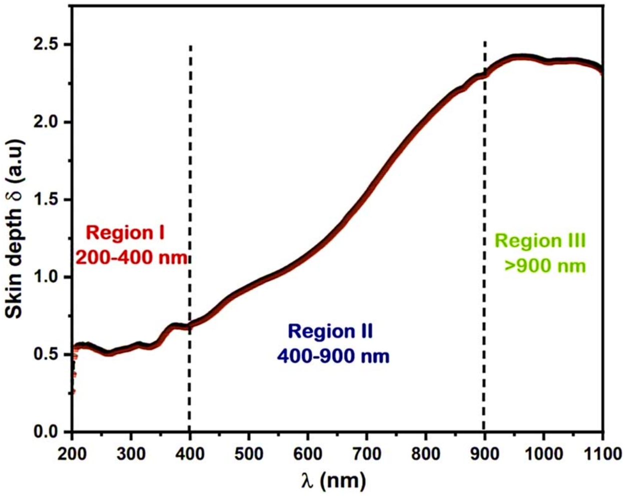

Fig. 14 Variation of penetration depth (δ) with wavelength (λ).

3.7.3. Penetration depth and optical extinction. The penetration depth (δ), or skin depth, defines how far incident light travels before diminishing to $1/e$ ($\sim$37%) of its original intensity, providing insights into surface and bulk properties. It depends on the material's absorption and scattering, with highly transparent materials exhibiting deeper penetration and highly absorbent ones showing shallow penetration. It is given by:[74]

$$\delta(\lambda) = \frac{1}{\alpha(\lambda)}$$

Fig. 14 illustrates the variation of (λ) across 200–1100 nm, revealing three distinct regions:

Region I (200–400 nm): high absorption indicates electronic transitions, effectively screening UV radiation. Region II (400–900 nm): increasing (λ) from visible to near-infrared suggests reduced absorbance and deeper penetration.

Region III (>900 nm): maximum penetration depth in the near-infrared implies minimal absorption.

These findings highlight the compound's strong UV-visible absorption, suitable for UV photodetectors and solar cells, while its increasing near-infrared transparency suggests potential in optical coatings and sensors.

The optical extinction coefficient (λ) describes the combined effect of absorption and scattering of light within the material, providing direct insight into its electronic transitions, and is expressed as:[75]

$$K(\lambda) = \frac{\lambda\alpha(\lambda)}{4\pi}$$

Fig. 15 shows the extinction spectrum of $(C_{10}H_{13}N_4)[BiBr_4]\cdot 2H_2O$, which displays seven characteristic peaks at 266, 296, 332, 342, 348, 418, and 540 nm, which can be grouped into three distinct energetic regions:

Region I (1.5–2.5 eV, 830–496 nm): exhibits moderate extinction dominated by the band-to-band electronic transitions, with a notable feature at 540 nm, attributed to transitions from the valence to conduction band across the Bi–Br network.

Region II (2.5–3.5 eV, 496–354 nm): shows stronger extinction with multiple peaks at 418, 348, 342, and 332 nm, corresponding to LMCT transitions and exciton–phonon coupling effects within the $[BiBr_4]_n$ chains.

Region III (3.5–6.0 eV, 354–207 nm): presents pronounced extinction in the near-to deep-UV range, with distinct peaks at

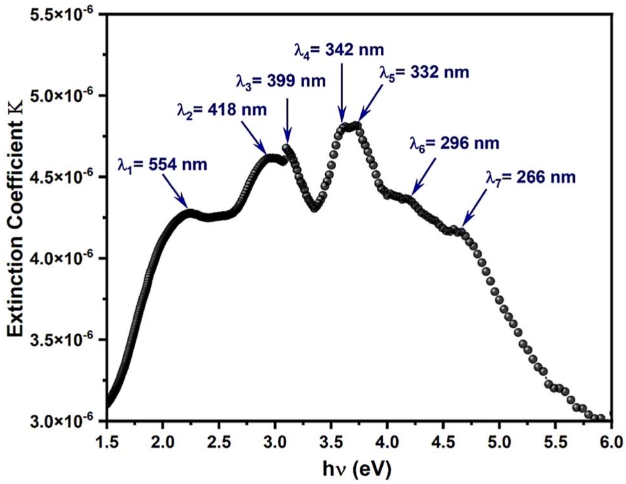

Fig. 15 Variation of extinction coefficient (K) as a function of wavelength.

296 and 266 nm, assigned to high-energy interband transitions involving deeper valence states of Br 4p and Bi 6s orbitals.

The compound thus demonstrates moderate optical extinction in the visible range and strong UV extinction, underscoring its suitability for UV photodetectors, optical filters, and radiation-blocking applications that rely on selective photon absorption and efficient charge generation.

3.8. Evolution of the refractive index

The refractive index (n) quantifies the interaction between incident light and the material's electronic structure, reflecting its polarizability and optical density. It was computed using the following relation:[76]

$$n(\lambda) = \frac{1 + R + \sqrt{4R - (1-R)^2 K^2}}{1 - R} = \frac{1 + R}{1 - R} + \sqrt{\frac{4R}{(1-R)^2} - K^2}$$

where R is the reflectance and k is the extinction coefficient. The spectral evolution of (λ) for the 1D bismuth-based hybrid (Fig. 16) shows three characteristic regions:

UV Region (200–400 nm): the refractive index starts near 2.0, with minimal variation, indicating low optical dispersion and limited photon–lattice coupling in the high-energy region.

UV-visible transition (400–700 nm): n gradually increases from ∼2.5 to 4.0, consistent with smooth dispersion behavior and stable optical transitions—an advantageous feature for waveguiding and photonic devices.

Visible-near-IR Region (700–1100 nm): a pronounced rise is observed, with n reaching ∼9.5 near 900–1000 nm, suggesting strong light–matter interaction, enhanced polarizability, and high electronic density associated with the heavy Bi(III) centers.

This significant refractive index in the near-IR range confirms the high optical density and polarizable electronic framework of the material, making it promising for nonlinear optical, photonic, and optoelectronic applications requiring strong field confinement.

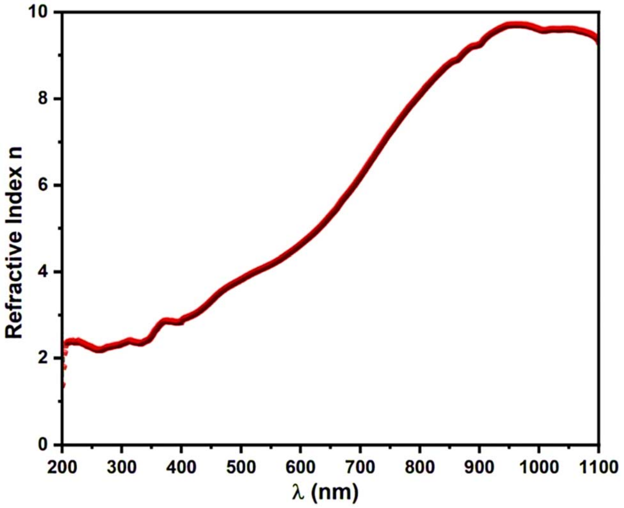

Fig. 16 Refractive index (n) plot.

3.9. Optical conductivity analysis

The optical conductivity (σ_{op}) describes the response of the material's charge carriers under an oscillating electromagnetic field, bridging its optical and electronic properties. It was calculated using the relation:

$$\sigma_{\text{op}} = \frac{\alpha(\lambda) n(\lambda) c}{4\pi k(\lambda)}$$

where α is the absorption coefficient, n the refractive index, k the extinction coefficient, and c the speed of light in vacuum

The $\sigma_{\text{op}}(\lambda)$ spectrum (Fig. 17) displays several prominent peaks across the UV-vis-NIR range, reflecting diverse electronic transitions. Key features are located at 209, 278, 316, 369, 478, 847, 883, and 919 nm, each corresponding to distinct optical excitations:

The strong UV peak at 209 nm indicates high optical conductivity and intense photon absorption, associated with large carrier concentration and efficient charge excitation.

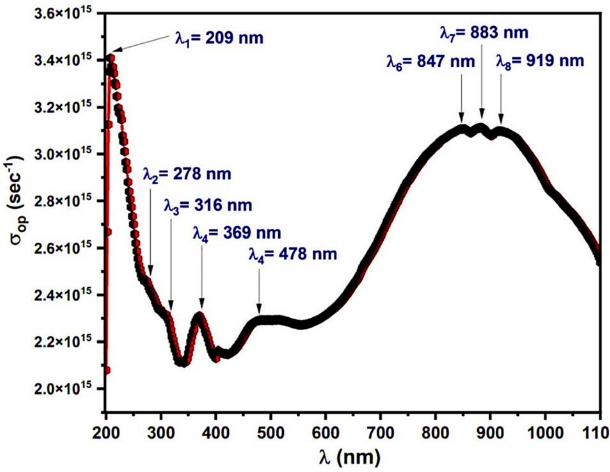

Fig. 17 Optical conductivity plot.

The visible region peaks (278–478 nm) correspond to LMCT and interband transitions, highlighting the participation of both Bi–Br and organic states in optical excitation processes.

The broad NIR feature (800–1000 nm), with maxima at 847, 883, and 919 nm, signifies sustained conductivity and delocalized carrier behavior over longer wavelengths.

Across the studied spectrum, σ_{op} maintains high values between 2.0×10^{15} and 3.6×10^{15} s^{-1}, indicating strong photon absorption, efficient charge-carrier generation, and rapid optical response. These findings affirm that $(C_{10}H_{13}N_4)[BiBr_4]\cdot 2H_2O$ exhibits excellent photoconductive and optoelectronic potential, making it an effective candidate for solar energy conversion, photoresponsive coatings, and broadband photonic devices.

The strong optical absorption and high optical conductivity (σ_{op}) values observed across the UV-visible region are a direct consequence of the SOC-influenced electronic structure and the low-dimensional inorganic framework. In indirect band-gap materials, such characteristics are particularly favorable for applications relying on efficient light harvesting and charge-carrier generation rather than radiative recombination. The combination of high σ_{op}, rapid optical response, and broad absorption profile supports the suitability of this hybrid material for absorption-driven optoelectronic applications, including photodetectors, photoresponsive coatings, and solar energy conversion layers. In this context, the proposed application perspectives arise from intrinsic structure–property relationships rather than from demonstrated device efficiencies.

3.10. Theoretical investigation

3.10.1. Frontier molecular orbital (FMO) analysis. The HOMO (highest occupied molecular orbital) and LUMO (lowest unoccupied molecular orbital) govern a compound's electronic, optical, and chemical behavior. HOMO represents electron-donating ability, while LUMO reflects electron-accepting capacity. A wide HOMO–LUMO gap indicates molecular "hardness" (low reactivity), whereas a narrow gap denotes "softness" (high reactivity). Ionization energy (EI = –E(HOMO)) and electron affinity (EA = –E(LUMO)) were derived directly from orbital energies. From Koopmans' theorem,[77,78] the chemical potential is given by $\mu = 1/2(\text{E(LUMO)} + \text{E(HOMO)})$, while global reactivity descriptors are defined as:

$$\eta = 1/2(E_{(\text{LUMO})} - E_{(\text{HOMO})}),\ \text{S} = \text{EI} / 2\eta,\ \omega = \mu^2 / 2\eta,\ \chi = 1/2(\text{EI} + \text{EA})$$

HOMO and LUMO energies were extracted using the DOS method, since Zero-DOS lacks accuracy for orbital energies. Band-gap values were analyzed from frontier orbitals, with the DOS spectrum generated in GaussSum 3.0 (ref. 79) (Fig. 18). Table 5.S lists orbital energies, gaps, and reactivity indices obtained with the choice of the mixed basis set simulations in water further characterized the electronic absorption profile. The low HOMO value highlights strong donor ability favorable for photovoltaics and OLEDs, while the LUMO indicates effective electron acceptance. The HOMO–LUMO gap determines stability and charge-transfer potential, relevant for optoelectronic devices. High EA stabilizes added electrons, enhancing photodetector and sensor performance, whereas high EI increases durability. The moderate dipole moment influences solubility and intermolecular interactions. Hardness/softness values balance stability with reactivity, crucial for catalysis, while a high electrophilicity index and the chemical potential provide global insight into reactivity.

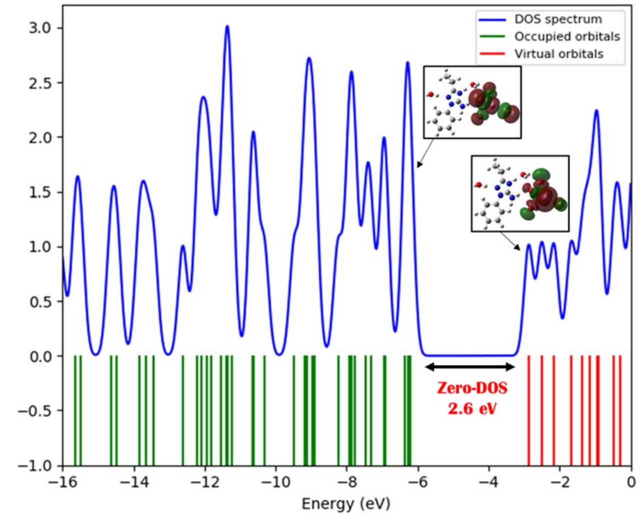

Fig. 18 Density of state (DOS) spectrum and the frontier molecular orbitals of the compound.

3.10.2. MEP, NCI-RDG, ELF, and LOL analyses. The hybrid compound $(C_{10}H_{13}N_4)[BiBr_4]\cdot 2H_2O$ has been analyzed through various computational techniques, including Molecular Electrostatic Potential (MEP), Non-Covalent Interaction reduced density gradient (NCI-RDG), Electron Localization Function (ELF), and Localized Orbital Locator (LOL). These methods provide a multifaceted view of the compound's electronic structure and bonding characteristics. The MEP analysis reveals the electrostatic potential distribution, highlighting reactive sites and intermolecular interactions. NCI-RDG mapping explores weak interactions such as van der Waals forces, hydrogen bonds, and steric repulsions. ELF and LOL analyses examine electronic localization and orbital characteristics, shedding light on delocalization and bonding frameworks. By integrating these tools, a comprehensive understanding of the compound's structural and electronic properties is achieved, supporting its potential applications in optoelectronics, materials design, and catalysis.

3.10.3. Molecular electrostatic potential MEP analysis. Molecular electrostatic potential (MEP) analysis provides crucial insights into electronic distribution, chemical reactivity, and intermolecular interactions. The MEP map for $(C_{10}H_{13}N_4)[BiBr_4]\cdot 2H_2O$ (Fig. 8.S) highlights electron-rich and electron-deficient regions. Negative potential areas (deep red) are concentrated around the bromine atoms in the $[BiBr_4]^-$ unit and the oxygen atoms of water molecules, indicating sites favorable for electrophilic interactions such as halogen and hydrogen bonding. Conversely, positive electrostatic potential (blue) is localized around hydrogen atoms bonded to nitrogen and carbon within the organic cation, suggesting susceptibility to nucleophilic attack and involvement in hydrogen bonding. The aromatic cation exhibits a nearly neutral potential with slight delocalization, hinting at possible π–π stacking interactions that may influence crystal packing. The Bi–Br coordination environment dominates the electrostatic landscape, illustrating the interactions between the organic cation and inorganic anion. Water molecules play a key role in modulating the local electronic environment by reinforcing the hydrogen-bonding network. The distinct potential regions emphasize the compound's ability to participate in halogen bonding, hydrogen bonding, and π-stacking, all of which contribute to its structural integrity and functional properties.

3.10.3.1 Non-covalent interaction NCI-RDG analysis. Non-Covalent Interaction (NCI) and Reduced Density Gradient (RDG) analyses provide insights into weak interactions influencing molecular stability. Fig. 9.S(a) shows the NCI isosurface for $(C_{10}H_{13}N_4)[BiBr_4]\cdot 2H_2O$, highlighting key interactions. Green isosurfaces indicate van der Waals forces around the aromatic moiety and water molecules, improving packing efficiency. Blue isosurfaces show strong hydrogen bonds between the organic cation, water oxygen atoms, and counterions, reinforcing the supramolecular structure. Red isosurfaces indicate steric repulsion around bulky bromine atoms and crowded organic regions, influencing molecular conformation. Fig. 9.S(b) displays the RDG scatterplot, which quantifies interactions by electron density analysis. Negative values correspond to hydrogen bonding, near-zero values to van der Waals forces, and positive values to steric hindrance, aligning with the NCI isosurface data. This analysis highlights the balance of attractive and repulsive forces governing the compound's stability. The NCI-RDG analysis reveals the role of hydrogen bonding, van der Waals forces, and steric effects in determining the compound's supramolecular structure and stability, offering key insights for evaluating its functional properties and designing related materials.

3.10.3.2 Electron localization function (ELF) and localized orbital locator (LOL) analyses. Fig. 10.S presents a three-dimensional visualization of the theoretical formula unit of $(C_{10}H_{13}N_4)[BiBr_4]\cdot 2H_2O$, shown across the (XY), (XZ), and (YZ) planes in Bohr units. This representation offers detailed insight into the spatial arrangement and structural orientation of the molecule's constituent atoms and functional groups. In the (XY) projection, the organic cation and $[BiBr_4]^-$ anion are clearly separated, with the Bi atom coordinated by four bromine atoms forming the shape of a seesaw geometry, shown by strong green bonds, highlighting the geometric symmetry of the anionic framework. The organic moiety, featuring a triazole ring system, is shown in a planar arrangement relative to the anion.

The (XZ) and (YZ) projections provide additional perspectives, revealing the slight tilt and angular positioning of the organic cation relative to the $[BiBr_4]^-$ anion. This anisotropic structure is influenced by intermolecular interactions such as hydrogen bonding and electrostatic forces. Water molecules are positioned strategically, mediating interactions between the organic and inorganic units and enhancing the compound's structural cohesion. These projections ensure a clear depiction of bond angles, distances, and molecular orientation, which are essential for assessing the compound's electronic and geometric properties. This figure is a valuable tool for interpreting both theoretical and experimental data, offering key insights into the compound's structural dynamics and potential applications in material science.

Fig. 11.S shows the Electron Localization Function (ELF) distribution of $(C_{10}H_{13}N_4)[BiBr_4]\cdot 2H_2O$ across the (XY), (XZ), and (YZ) planes, revealing electron-pair localization and bonding. ELF isosurfaces and 2D maps, color-coded from blue (low) to red (high), highlight electronic regions. In the (XY) plane, strong localization around the bromine atoms in $[BiBr_4]^-$ (red) indicates lone pairs, with moderate localization near Bi reflecting its coordination role. The organic moiety shows electron density around the nitrogen atoms in the triazole ring. The (XZ) and (YZ) planes confirm delocalized covalent bonds in the organic unit and localized density in the inorganic part. Hydrogen bonding effects appear as low to moderate localization bridging the organic and inorganic components. This ELF analysis provides insights into the compound's stability, reactivity, and potential as a functional material.

Fig. 12.S presents the Localized Orbital Locator (LOL) distribution in the (XY), (XZ), and (YZ) planes, mapping orbital localization. High LOL values around nitrogen atoms in the triazole moiety and bromine atoms in $[BiBr_4]^-$ indicate localized lone pairs, while Bi shows lower localization, reflecting its coordination. The (XZ) and (YZ) planes further distinguish lone pairs from delocalized covalent bonds. Low LOL values around water molecules suggest their role in hydrogen bonding. This LOL analysis complements the ELF study, offering key insights into electronic structure and bonding behavior.

3.11. Hirshfeld surface analysis (HSA)

A Hirshfeld surface analysis was performed using CrystalExplorer 21.5 to assess the intermolecular interactions in the compound, resulting in 2D fingerprint plots. Fig. 13.S displays the 3D surface representations of the molecule with the normalized dnorm function (Fig. 13.S(a)) and shape index (Fig. 13.S(b)). The Hirshfeld surface (Fig. 13.S(a)), color-coded in red, blue, and white, reflects the relative surface area of each point based on the (d_e, d_i) pair. Blue areas indicate minimal surface contribution, while red signifies significant contribution. The dnorm function, a measure of intermolecular interactions, shows regions of close contact in red, indicating hydrogen bond donor–acceptor interactions, such as N–H⋯O, O–H⋯N, and O–H⋯Br hydrogen bonds. White spots highlight H/H contacts, further indicating the diversity of interactions within the crystal structure. Fig. 13.S(b) illustrates the shape of the molecule, with adjacent blue and red triangles confirming π interactions around the organic molecule's aromatic rings. Fig. 14.S presents the 2D fingerprint plot of the total contacts contributing to the Hirshfeld surface. It focuses on the 0.6 to 2.8 Å distance range, showing the contributions of different intermolecular interactions. The plot highlights H/Br interactions as the dominant contribution, constituting 55% of the total, followed by H···H interactions (19.1%). These results emphasize the importance of hydrogen bonding in stabilizing the hybrid material, affecting properties such as chemical stability, mechanical strength, and optical transparency. The CrystalExplorer 21.5 tool also visualized crystal voids, impacting the material's solubility, density, and mechanical properties. Fig. 15.S shows a void volume of 145.56 Å^3, occupying 7.74% of the unit cell's total volume. Despite the presence of voids, the material exhibits enhanced compactness, suggesting higher density and mechanical strength, likely improving thermal conductivity and optical transparency. These characteristics, including minimal void presence, contribute to the material's robustness and optical clarity, with potential verification through Thermal Gravimetric Analysis (TGA).

4. Conclusion

The present study reports the successful synthesis and in-depth characterization of the one-dimensional bromobismuthate(III) hybrid $(C_{10}H_{13}N_4)[BiBr_4]\cdot 2H_2O$, offering a unified understanding of its crystal structure, vibrational behavior, and optical performance. The material crystallizes in the monoclinic space group $P2_1/n$, featuring edge-sharing $BiBr_6$ octahedra forming continuous $[BiBr_4]_n^{n-}$ chains stabilized through a three-dimensional network of hydrogen bonds and π–π stacking, giving rise to a highly cohesive framework. Thermal analysis confirmed exceptional stability up to 275 °C, validating its structural integrity and suitability for device-level implementation.

FTIR and Raman analyses identified distinct signatures of the organic and inorganic components, confirming strong cation–anion coupling and coherent lattice dynamics. Optical spectroscopy revealed an indirect band gap (2.56 eV) consistent with DFT predictions, reflecting the influence of spin–orbit coupling and structural anisotropy inherent to Bi-based 1D systems. Diffuse reflectance, UV-vis, and PL spectra jointly demonstrated efficient light absorption and a broad blue–violet emission, establishing its semiconducting nature. The CIE 1976 colorimetry confirmed high saturation and chromatic stability, making the compound a strong candidate for light-emitting diodes (LEDs) and photodetectors.

Overall, the combined influence of the heavy Bi^{3+} center, strong spin–orbit coupling, low-dimensional inorganic framework, and rationally selected non-commercial organic cation gives rise to an indirect band-gap electronic structure, strong optical absorption, and pronounced photoresponse. These interconnected structural and physical features provide a coherent basis for the proposed absorption-based optoelectronic applications and underline the value of the present system as a model platform for structure–property investigations in low-dimensional bismuth halide hybrids.

Advanced DFT analyses provided complementary microscopic insights: Electron Localization Function (ELF) mapping highlighted the localization of Bi–Br bonding and the stereochemical activity of the Bi 6 s^2 lone pair; Reduced Density Gradient (RDG) and Non-Covalent Interaction (NCI) plots revealed dominant hydrogen bonding, π–π stacking, and van der Waals interactions, which underpin the crystal's stability. Electrostatic potential (ESP) mapping confirmed strong charge separation, with the organic cation acting as a donor and the $[BiBr_4]_n^{n-}$ framework as an acceptor, enabling efficient charge transfer.

Collectively, these results position $(C_{10}H_{13}N_4)[BiBr_4]\cdot 2H_2O$ as a structurally robust and optically active hybrid material, capable of addressing key challenges in optoelectronics, photovoltaics, and photonic energy conversion. Future efforts may focus on band gap engineering through cationic substitution, pressure modulation, or dimensional control, paving the way for enhanced performance in next-generation lead-free semiconductor technologies.

Conflicts of interest

The authors declare that they have no known competing financial interests or personal relationships that could have appeared to influence the work reported in this paper.

Data availability

The authors confirm that the data supporting the findings of this study are available within the article.

CCDC 2387887 contains the supplementary crystallographic data for this paper.[80]

Supplementary information (SI) is available. See DOI: https://doi.org/10.1039/d5ra09435f.

Acknowledgements

I would like to thank the Principal Engineer of the physics department of the Faculty of Sciences of Sfax Mrs DAMMAK Sameh for carrying out the chemical analyses by FTIR spectroscopy and UV-visible spectroscopy.

References

1 L. Liang and P. Gao, *Adv. Sci.*, 2018, **5**, 1700331.
2 L. Etgar, *MRS Bull.*, 2015, **40**, 674.
3 N. J. Jeon, J. H. Noh, W. S. Yang, Y. C. Kim, S. Ryu, J. Seo and S. Il Seok, *Nature*, 2015, **517**, 476.
4 W. S. Yang, J. H. Noh, N. J. Jeon, Y. C. Kim, S. Ryu, J. Seo and S. Il Seok, *Science*, 2015, **348**, 1234.
5 M. Saliba, T. Matsui, J.-Y. Seo, K. Domanski, J.-P. Correa-Baena, N. Mohammad, S. M. Zakeeruddin, W. Tress, A. Abate, A. Hagfeldt and M. Gratzel, *Energy Environ. Sci.*, 2016, **9**, 1989.
6 G. C. Papavassiliou, G. A. Mousdis, A. Terzis and C. P. Raptopoulou, *Z. Naturforsch., B:J. Chem. Sci.*, 2003, **58**, 815.
7 A. Samet, H. Boughzala, H. Khemakhem and Y. Abid, *J. Mol. Struct.*, 2010, **984**, 23.
8 A. Vassilakopoulou, D. Papadatos, I. Zakouras and I. Koutselas, *J. Alloys Compd.*, 2017, **692**, 589.

9 A. Yangui, S. Pillet, E. Bendeif, A. Lusson, S. Triki, Y. Abid and K. Boukheddaden, *ACS Photonics*, 2018, **5**, 1599.

10 W. Zhang, K. Tao, C. Ji, Z. Sun, S. Han, J. Zhang, Z. Wu and J. Luo, *Inorg. Chem.*, 2018, **57**, 4239.

11 G. Lanty, A. Bréhier, R. Parashkov, J. S. Lauret and E. Deleporte, *New J. Phys.*, 2008, **10**, 065007.

12 C. R. Kagan, D. B. Mitzi and C. D. Dimitrakopoulos, *Science*, 1999, **286**, 945.

13 S. Pandey, T. Chattopadhyay, S. Dev, Y. Patil, C. L. Carpenter-Warren and C. Sinha, *Polyhedron*, 2020, **179**, 114335.

14 A. Gągor, M. Węcławik, B. Bondzior and R. Jakubas, *CrystEngComm*, 2015, **17**, 3286.

15 A. J. Dennington and M. T. Weller, *Dalton Trans.*, 2018, **47**, 3469.

16 S. Pandey, A. P. Andrews and A. Venugopal, *Dalton Trans.*, 2016, **45**, 8705.

17 W. Ning and F. Gao, *Adv. Mater.*, 2019, **31**, e1900326.

18 C. Wu, Q. Zhang, G. Liu, Z. Zhang, D. Wang, B. Qu, Z. Chen and L. Xiao, *Adv. Energy Mater.*, 2019, **10**, 1902496.

19 U. H. Hamdeh, B. J. Ryan, R. D. Nelson, M. Zembrzuski, J. Slobidsky, K. J. Prince, I. Cleveland, A. Vela-Ramirez, A. C. Hillier and M. G. Panthani, *J. Phys. Chem. Lett.*, 2019, **10**, 3134.

20 X. Huang, S. Huang, P. Biswas and R. Mishra, *J. Phys. Chem. C*, 2016, **120**, 28924.

21 X. G. Zhao, D. Yang, J. C. Ren, Y. Sun, Z. Xiao and L. Zhang, *Joule*, 2018, **2**, 1662.

22 S. A. Adonin, I. D. Gorokh, D. G. Samsonenko, M. N. Sokolov and V. P. Fedin, *Chem. Commun.*, 2016, **52**, 5061.

23 X. H. Zhu, N. Mercier, M. Allain, P. Frere, P. Blanchard and J. Roncali, *J. Solid State Chem.*, 2004, **177**, 1067.

24 B.-W. Park, B. Philippe, X. Zhang, H. Rensmo, G. Boschloo and E. M. J. Johansson, *Adv. Mater.*, 2015, **27**, 6806.

25 M. Pazoki, M. B. Johansson, H. Zhu, P. Broqvist, T. Edvinsson, G. Boschloo and E. M. J. Johansson, *J. Phys. Chem. C*, 2016, **120**, 29039.

26 M. B. Johansson, H. Zhu and E. M. J. Johansson, *J. Phys. Chem. Lett.*, 2016, **7**, 3467.

27 Z. Zhang, X. Li, X. Xia, Z. Wang, Z. Huang, B. Lei and Y. Gao, *J. Phys. Chem. Lett.*, 2017, **8**, 4300.

28 R. Jakubas, A. Piecha, A. Pietraszko and G. Bator, *Phys. Rev. B*, 2005, **72**, 104107.

29 N. Leblanc, N. Mercier, L. Zorina, S. Simonov, P. A. Senzier and C. Pasquier, *J. Am. Chem. Soc.*, 2011, **133**, 14924.

30 O. V. Dolomanov, L. J. Bourhis, R. J. Gildea, J. A. K. Howard and H. Puschmann, *J. Appl. Crystallogr.*, 2009, **42**, 339.

31 G. M. Sheldrick, *Acta Crystallogr., Sect. B:Struct. Sci., Cryst. Eng. Mater.*, 2015, **71**, 3.

32 G. M. Sheldrick, *Acta Crystallogr. C*, 2015, **71**, 3.

33 K. Brandenburg and H. Putz, *Diamond Crystal Analysis Software*, Crystal Impact GbR, Bonn, Germany, 1999.

34 L. Checinska, S. Grabowsky, M. Malecka, A. J. Rybarczyk-Pirek, A. Józwiak, C. Paulmann and P. Luger, *Acta Crystallogr. B Struct. Crystallogr. Cryst. Chem.*, 2011, **67**, 569.

35 S. K. Seth, D. Sarkar, A. D. Jana and T. Kar, *Cryst. Growth*, 2011, **11**, 4837.

36 S. K. Seth, D. Sarkar and T. Kar, *CrystEngComm*, 2011, **13**, 4528.

37 P. Manna, S. K. Seth, A. Das, J. Hemming, R. Prendergast, M. Helliwell, S. R. Choudhury, A. Frontera and S. Mukhopadhyay, *Inorg. Chem.*, 2012, **51**, 3557.

38 R. Spackman, M. J. Turner, J. J. McKinnon, S. K. Wolff, D. J. Grimwood, D. Jayatilaka and M. A. Spackman, *J. Appl. Crystallogr.*, 2021, **54**, 1006.

39 M. A. Spackman and J. J. McKinnon, *CrystEngComm*, 2002, **4**, 378.

40 J. J. McKinnon, M. A. Spackman and A. S. Mitchell, *Acta Crystallogr. B*, 2004, **60**, 627.

41 S. K. Seth, G. C. Maity and T. Kar, *J. Mol. Struct.*, 2011, **1000**, 120.

42 A. L. Rohl, M. Moret, W. Kaminsky, K. Claborn, J. J. McKinnon and B. Kahr, *Cryst. Growth*, 2008, **8**, 4517.

43 J. J. McKinnon, D. Jayatilaka and M. A. Spackman, *Chem. Commun.*, 2007, **37**, 3814.

44 A. Tounsi, S. Elleuch, B. Hamdi, R. Zouari and A. Ben Salah, *J. Mol. Struct.*, 2017, **1141**, 512.

45 N. Zhanpeisov, M. Matsuoka, H. Yamashita and M. Anpo, *J. Phys. Chem. B*, 1998, **102**, 6915.

46 M. J. Frisch, G. W. Trucks, H. B. Schlegel, G. E. Scuseria, M. A. Robb, J. R. Cheeseman, G. Scalmani, V. Barone, B. Mennucci, G. A. Petersson, H. Nakatsuji, M. Caricato, X. Li, H. P. Hratchian, A. F. Izmaylov, J. Bloino, G. Zheng, J. L. Sonnenberg, M. Hada, M. Ehara, K. Toyota, R. Fukuda, J. Hasegawa, M. Ishida, T. Nakajima, Y. Honda, O. Kitao, H. Nakai, T. Vreven, J. A. Montgomery Jr, J. E. Peralta, F. Ogliaro, M. Bearpark, J. J. Heyd, E. N. Brothers, K. N. Kudin, V. N. Staroverov, R. Kobayashi, J. Normand, K. Raghavachari, A. Rendell, J. C. Burant, S. S. Iyengar, J. Tomasi, M. Cossi, N. Rega, J. M. Millam, M. Klene, C. Adamo, R. Cammi, J. W. Ochterski, R. L. Martin, K. Morokuma, O. Farkas, J. B. Foresman and D. J. Fox, *Gaussian 09, Revision E.01*, Gaussian, Inc., Wallingford CT, 2013.

47 N. Nicklass, M. Dolg, H. Stoll and H. Preuss, *J. Chem. Phys.*, 1995, **102**, 8942.

48 R. Dennington, T. A. Keith and J. M. Millam, *GaussView, Version 5*, Semichem Inc., Shawnee Mission, KS, 2009.

49 T. Lu and F. Chen, Multiwfn: A multifunctional wavefunction analyzer, *J. Mol. Struct.*, 2012, **1006**, 84–92.

50 I. D. Brown, *Acta Crystallogr., Sect. B:Struct. Sci., Cryst. Eng. Mater.*, 1976, **32**, 24.

51 M. Blessing, *Acta Crystallogr., Sect. B:Struct. Sci., Cryst. Eng. Mater.*, 1976, **32**, 25.

52 J. Tauc, *Mater. Res. Bull.*, 1968, **3**, 37.

53 J. I. Pankove, *Optical Processes in Semiconductors*, Prentice-Hall, New Jersey, 1971.

54 B. V. Bukvetskii, T. V. Sedakova and A. G. Mirochnik, *J. Struct. Chem.*, 2009, **50**, 322.

55 N. Leblanc, M. Allain, N. Mercier and L. Sanguinet, *Cryst. Growth Des.*, 2011, **11**, 2064.

56 Y. J. Wang and L. Xu, *J. Mol. Struct.*, 2008, **875**, 570–576.

57 H. Ferjani, H. Boughzala and A. Driss, *Acta Crystallogr. E*, 2012, **68**, m615.

58 C. Hrizi, A. Trigui, Y. Abid, N. Chniba-Boudjada, P. Bordet and S. Chaabouni, *J. Solid State Chem.*, 2011, **184**, 3336.
59 Mercury CSD 3.0.1 (Build RC6), Cambridge Crystallographic Data Centre (CCDC), 2011.
60 A. S. Rao, U. Baruah and S. K. Das, *Inorg. Chim. Acta*, 2011, **372**, 206.
61 A. Vogler and A. Paukner, *Coord. Chem. Rev.*, 1990, **97**, 285.
62 A. Vogler and H. Nikol, *Pure Appl. Chem.*, 1992, **64**, 1311.
63 D. S. Shtarev, M. I. Balanov, A. Ju. Major, A. V. Gerasimenko, R. Kevorkyants, D. A. Zharovov, K. M. Bulanin, D. V. Pankin, A. V. Rudakova, D. A. Chaplygina, N. I. Selivanov and A. V. Emeline, *J. Mater. Chem. C*, 2024, **12**, 262–275.
64 N. Navarro, R. Nelson, K. Gallardo and R. Castillo, *Molecules*, 2024, **29**, 2141.
65 A. O. Murzin, A. Yu. Samsonova, C. C. Stoumpos, N. I. Selivanov, A. V. Emeline and Y. V. Kapitonov, *Molecules*, 2023, **28**, 350.
66 R. Mguedla, A. Ben Jazia, O. Kharrat, H. Taktak, S. Souissi, K. Kammoun, K. Khirouni and W. Boujelben, *Opt. Mater.*, 2020, **101**, 109742.
67 R. E. Marotti, D. N. Guerra, C. Bello, G. Machado and E. A. Dalchiele, *Sol. Energy Mater. Sol. Cells*, 2004, **82**, 85.
68 M. Hafez, I. S. Yahia and S. Taha, *Spectrochim. Acta A Mol. Biomol. Spectrosc.*, 2014, **127**, 521.
69 K. SowriBabun, A. Ramachandra Reddy, Ch. Sujatha and K. Venugopal Reddy, *Ceram. Int.*, 2013, **39**, 3055.
70 A. H. Slavney, T. Hu, A. M. Lindenberg and H. I. Karunadasa, *J. Am. Chem. Soc.*, 2016, **138**, 213.
71 G. D. Cody, in *Semiconductors and Semimetals*, ed. J. I. Pankove, Academic Press, Orlando, 1984, vol. 21.
72 A. S. Hassanien and A. A. Akl, *J. Alloys Compd.*, 2015, **648**, 280.
73 H. R. Shakur, *Phys. E*, 2011, **44**, 641.
74 E. Caponetti, L. Pedone, D. Chillura Martino, V. Panto and V. Turco Liveri, *Mater. Sci. Eng., C*, 2003, **23**, 531.
75 N. Tounsi, A. Barhoumi, F. C. Akkari, M. Kanzari, H. Guermazi and S. Guermazi, *Vacuum*, 2015, **121**, 9.
76 S. R. Chalana, V. Ganesan and V. P. Mahadevan Pillai, *AIP Adv.*, 2015, **5**, 107207.
77 R. K. Singh, S. K. Verma and P. D. Sharma, *Int. J. ChemTech Res.*, 2011, **3**, 1571.
78 C. G. Zhan, J. A. Nichols and D. A. Dixon, *J. Phys. Chem. A*, 2003, **107**, 4184.
79 N. M. O'Boyle, A. L. Tenderholt and K. M. Langner, *J. Comput. Chem.*, 2008, **29**, 839.
80 CCDC 2387887: Experimental Crystal Structure Determination, 2026, DOI: 10.5517/ccdc.csd.cc2l4sm5.